ACS OMEGA

Open Access

http://pubs.acs.org/journal/acsodf

Article

Deciphering the Reaction Cycle Mechanisms and Key Reaction Factors of Monochlorosilane by Disproportionation of Dichlorosilane via Experiments and Density Functional Theory

Ke Sun, Qiuyun Mao,* Jianyun Zheng, Jianhua Liu, Zhenjun Yuan, Guangan Gu, Guopeng Li, Ye Wan,* and Qifan Zhong*

Cite This: *ACS Omega* 2025, 10, 19480−19490

Read Online

ACCESS | Metrics & More | Article Recommendations | Supporting Information

ABSTRACT: Monochlorosilane (MCS) is an important silicon-based precursor for the fabrication of semiconductors and integrated circuits. The MCS production partly depends on the catalytic disproportionation of dichlorosilane (DCS). The DCS disproportionation has been critical yet challenging due to the involvement of multiple reversible reactions and other byproducts, often resulting in suboptimal yields of MCS. This investigation explored the sensitive conditions and key controlling factors affecting MCS yield in DCS disproportionation using gas chromatography−mass spectrometry (GC−MS). With increasing feed rates, the temperature requirement for DCS disproportionation gradually increased, and the sensitivity became significantly enhanced at high pressures. The optimal reaction conditions were 0.2 kg/h, 323.15 K, and 0.3 MPa. More importantly, density functional theory (DFT) calculations revealed the complete reaction cycle pathways of MCS generation. In these pathways, DCS dehydrogenation was identified as the rate-determining step, exhibiting the antagonistic effect with MCS disproportionation. The $SiHCl_3$−SiH_2Cl^- species, acting as the key intermediate, decomposed after promoting chlorine transfer to produce MCS and trichlorosilane (TCS). Furthermore, chloride ions, as byproducts, not only removed reactants but also acted as the chlorine source. This study provides significant theoretical guidance for the precise control of chlorosilane disproportionation reactions and the design of related catalysts.

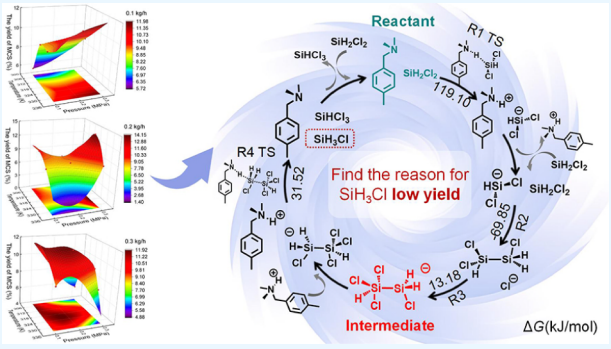

1. INTRODUCTION

Monochlorosilane (MCS), an important silicon-based precursor, is widely used in semiconductor epitaxy, chemical vapor deposition processes, and the organosilicon industry.[1−5] The synthesis methods of MCS primarily include the condensation of silanes and dichlorosilane (DCS) and the disproportionation of DCS (eqs 1 and 2).[6] In both methods, the DCS disproportionation process plays a critical role in silane production via chlorosilane disproportionation (commonly known as the Union Carbide Corporation Silane Process or UCC method[7]). The UCC method involves the progressive dechlorination/hydrogenation of trichlorosilane, sequentially yielding DCS, MCS, and ultimately silane. This method holds significant industrial importance for chlorosilane manufacturing. Various catalysts are available for the chlorosilane disproportionation process, such as aluminum chloride,[8,9] alumina,[10,11] and nitrogen-containing anion exchange resins.[12,13] Among these, nitrogen-containing anion exchange resins (e.g., Amberlyst A21 and Amberlyst A26) are optimal due to high reactivity, ease of separation and lack of impurities. However, the disproportionation of DCS usually shows relatively low MCS yield due to multiple, continuous, and reversible disproportionation reactions of chlorosilanes (eqs 1−3).[14] On the other hand, MCS and trichlorosilane (TCS) can be further disproportionated by the same catalysts to generate a wider variety of chlorosilane products. These factors make the chlorosilane disproportionation system extremely complex, necessitating the complete reaction pathway and key reaction parameters for selectively and effectively obtaining the target products (e.g., MCS). In addition, the disproportionation reactions among various chlorosilanes are rapid and almost simultaneous,[15] which undoubtedly increases the difficulty of experimentally exploring the complete reaction pathway.

$$SiH_4 + SiH_2Cl_2 \leftrightarrow 2SiH_3Cl \quad (1)$$

Received: December 23, 2024
Revised: April 10, 2025
Accepted: April 29, 2025
Published: May 8, 2025

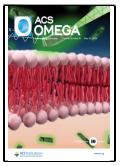

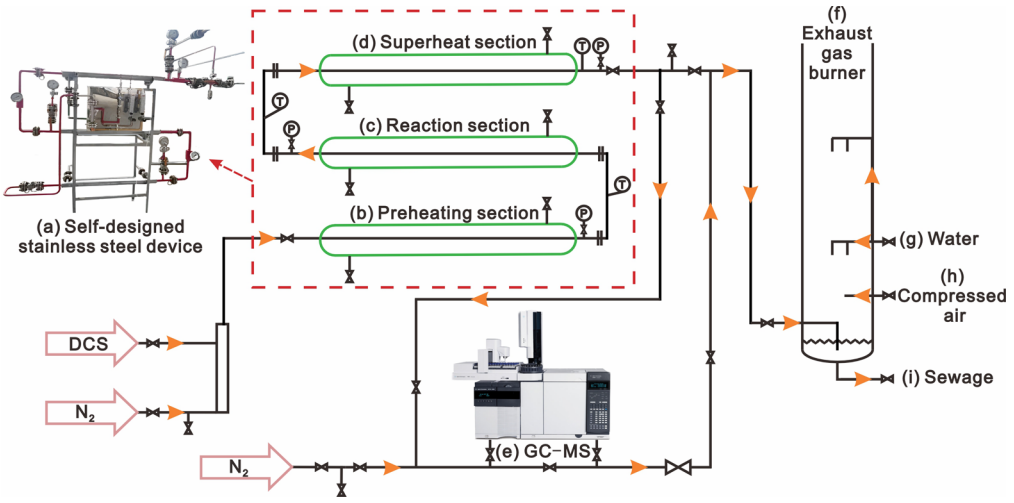

Figure 1. Experimental setup for DCS disproportionation to MCS consisted of a self-designed stainless steel device (a), GC–MS (e), and the exhaust gas burner (f). The self-designed stainless steel device comprised the preheating section (b), the reaction section (c), and the superheat section (d). The exhaust gas burner utilized water (g) for cooling and compressed air (h) for combustion support, ultimately discharging the sewage (i).

$$2SiH_2Cl_2 \leftrightarrow SiH_3Cl + SiHCl_3 \quad (2)$$

$$2SiHCl_3 \leftrightarrow SiCl_4 + SiH_2Cl_2 \quad (3)$$

The complex reaction pathway of chlorosilane disproportionation has captivated numerous scholars. Union Carbide Corporation has used isotopic tracing experiments (deuterium labeling) to explore the proton transfer among multiple molecules in chlorosilane disproportionation with Amberlyst A21.[16] Besides, Ring et al.[17] and Vorotyntsev et al.[15,18] have demonstrated the formation of intermediates (e.g., $(CH_3)_3NH^+$ and $SiCl_3^+$) in the disproportionation reaction of TCS and the protonation of nitrogen atoms by using infrared spectroscopy, X-ray analysis, and in-line mass monitoring, respectively. However, the key intermediates could not be fully characterized through experimental detection due to the rapid and complex nature of the reaction, as well as the limitations posed by mass spectral overlap. Moreover, chlorosilanes are flammable, explosive, corrosive, and toxic,[19] posing serious difficulties for experimental feasibility. Thus, relying solely on experiments to reveal a comprehensive reaction pathway for the disproportionation of chlorosilanes cannot be achieved, necessitating the integration of theoretical calculations for a thorough investigation.

Density functional theory (DFT) calculations play an active role in explaining material properties, guiding the experimental synthesis, and predicting new material applications due to their capability to analyze comprehensively at atomic and molecular scales.[20−23] Boychuk et al.[24] have tested the performance of 54 DFT functions in combination with three triple-ζ basis sets, with the average percentage error below 2% and the minimum relative deviation of 0.1 kcal/mol. Moreover, the reliability of DFT calculations has been validated by various experimental processes. Xu et al.[25] have used DFT calculations to screen for Cu-doped TiO_2 as a good catalyst and verified the results through numerous CO_2 reduction experiments and other analytical methods. Coin et al.[26] have confirmed the synthetic pathway of amidines proposed by DFT and experimental characterizations like X-ray and NMR analysis. More importantly, DFT can be applied to investigate the reaction systems for the synthesis of silicon-based materials. Stanford et al.[27] have elucidated the reaction pathways of disilene/silylsilylene isomerizations through DFT calculations. In summary, DFT calculations could accurately and feasibly explore the reaction pathway of chlorosilanes, contributing to the comprehensive understanding of the reaction essence, especially in cases where conducting experiments is challenging.

To address the intricate and unclear reaction mechanism of chlorosilane disproportionation, the catalytic disproportionation reaction of DCS was focused on. And the key factors for the synthesis of MCS were explored via experiments and DFT calculations. From the standpoint of material cycles, this work introduced comprehensive DCS catalytic disproportionation cycle pathways, elucidated the mechanisms of side reactions that influenced yield, and identified the key factors affecting the reaction.

2. METHODS

2.1. Experimental and Analysis Methods. The DCS and N_2 used in the experiments were provided by Luoyang China Silicon Corporation Ltd., with a purity of 99.9 wt %. Amberlyst A21 was obtained from Shanghai Rohm and Haas Chemical Corporation. The experimental setup for DCS disproportionation to MCS, as shown in Figure 1, consisted of a self-designed stainless steel device, an Agilent 7890B-5977 gas chromatography–mass spectrometer (GC–MS), and an exhaust gas burner.

The self-designed stainless steel device comprised the preheating section, the reaction section, and the superheat section. The preheating section, the reaction section, and the superheat section were all constructed using stainless steel pipes that measured 2.54 cm in diameter and 1.50 m in length, with hot water jackets enclosing the outer surfaces of the pipes. The hot water jackets utilized a volumetric flow meter to control the hot water flow, and a thermometer monitored the heating temperature. All pipes in the stainless steel device underwent electrolytic polishing to remove oil, rust, and other impurities from the inner surfaces. This process ensured internal cleanliness and maintained surface roughness below

https://doi.org/10.1021/acsomega.4c11528
ACS Omega 2025, 10, 19480−19490

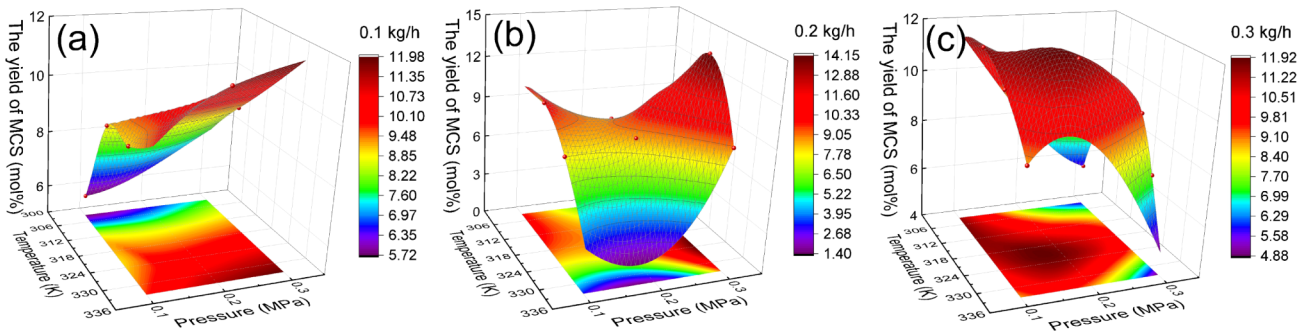

Figure 2. Effect of temperature and pressure variations on MCS yield at feed rates of 0.1 kg/h (a), 0.2 kg/h (b), and 0.3 kg/h (c) within the temperature range of 303.15 to 333.15 K and pressure range of 0.1 to 0.3 MPa.

0.4 μm. The pipes were connected using 316L stainless steel welded joints.

During the experiment, DCS and N_2 were preheated to the reaction temperature and pressure in the preheating section. The reaction temperature and pressure were regulated by a Programmable Logic Controller (PLC), and gas flow was controlled using diaphragm valves. Subsequently, DCS underwent the disproportionation reaction in the reaction section, catalyzed by 200 g of Amberlyst A21 catalyst. The reaction products entered the superheat section and were heated to 343.15 K to maintain a gaseous state, preventing stagnation in the pipes. The products exiting the superheat section flowed through a heated transfer line, maintained at 353.15 K to avoid condensation, and were continuously introduced into the GC−MS. The sample required for GC−MS detection was delivered via a sampling valve equipped with a 0.5 mL loop. The sampling valve was programmed to transfer gaseous samples to the GC−MS every 30 s. The GC−MS quantitatively analyzed components such as N_2, silane, MCS, DCS, TCS, and silicon tetrachloride using an Agilent gas chromatograph program for temperature ramping and component separation, with a stationary phase of 100% dimethylpolysiloxane in the chromatographic column. GC−MS sampling continued at 30-s intervals, and the sampling valve and transfer line were purged with N_2 for 10 s between injections to prevent cross-contamination. Sampling and analysis ceased when three consecutive measurements showed the MCS concentration variation of less than 2%, indicating that the reaction reached a stable equilibrium. The average of these three measurements served as the final result for the given conditions.

Finally, the exhaust gas passed through pipes into the exhaust gas burner, where it underwent combustion for harmless treatment. The top of the exhaust gas burner employed electric heating to raise the chamber temperature to 1123.15 K, with compressed air at a pressure of 0.5 MPa introduced to support combustion. The chamber of the exhaust gas burner was cooled using closed-loop water at a pressure of 0.5 MPa and a temperature of 288.15 K. The oxides generated from the combustion of the exhaust gas fell into the water washing tank for precipitation. Afterward, the water from the tank was filtered and discharged as the sewage. Additionally, the combusted exhaust gas required alkali scrubbing to meet emission standards before release.

The effects of temperature (303.15−333.15 K), pressure (0.1−0.3 MPa), and feed rate (0.1−0.3 kg/h) on the MCS yield were determined through experiments. The temperature range investigated in the experiments was determined based on process parameters established in previous studies,[16,28,29] The pressure range and DCS feed rate range were selected according to the processing capacity of the existing experimental setup.

2.2. DFT Calculations. Amberlyst A21 was simplified to $CH_3C_6H_4CH_2N(CH_3)_2$ in the calculations.[30] The DFT calculations of the reaction process between $CH_3C_6H_4CH_2N(CH_3)_2$ and DCS at 333.15 K were conducted using Gaussian 16 software.[31] The B3LYP-D3(BJ)/6-311G(d,p)[32] method was used for the optimization of molecular structure, vibrational analysis, and transition state search, while electronic energies were calculated using the CCSD(T)/cc-pVTZ[33] method. Intrinsic reaction coordinate (IRC) calculations were conducted to ensure the identified potential energy surface (PES) saddle points accurately connected reactants and products.[34] Gibbs free energy barriers at 333.15 K were calculated using thermodynamic composite methods G4[35] or G4MP2.[36] The G4MP2 method was employed for systems with more than 20 atoms. Reaction rate constants k were computed based on Transition State Theory (TST) (eqs 4−7),[37] facilitating the comparison of reaction feasibility and identification of the rate-determining step.

$$k = \sigma \frac{k_B T}{h} \left(\frac{RT}{P_0} \right)^{\Delta n} e^{-\Delta G^{0,\neq}(T)/(k_B T)} \tag{4}$$

$$\Delta G^{0,\neq}(T) = G^0_{TS}(T) - G^0_{Reactant}(T) \tag{5}$$

$$\sigma = \frac{\sigma_{rot,R}}{\sigma_{rot,TS}} \tag{6}$$

$$\Delta n = n - 1 \tag{7}$$

where k is the reaction rate constant, σ is the degeneracy of the reaction path, k_B is the Boltzmann constant, R represents the ideal gas constant, T corresponds to the temperature, P_0 is the standard atmospheric pressure, $\Delta G^{0,\neq}(T)$ is the free energy barrier at the standard state concentration (1 bar), n is the moles of reactants. $\sigma_{rot,R}$ and $\sigma_{rot,TS}$ are the rotational symmetry numbers for the reactants and the transition state, respectively.

Additionally, charge distributions of molecules or ions were calculated through the natural population analysis (NPA), and wave function analyses such as bond order and dual descriptor were conducted using the Multiwfn program.[38]

3. RESULTS AND DISCUSSION

To gain deeper insights into the disproportionation of DCS and identify optimal reaction conditions, experiments were conducted to investigate the effects of varying temperatures

https://doi.org/10.1021/acsomega.4c11528
ACS Omega 2025, 10, 19480−19490

(303.15−333.15 K) and pressures (0.1−0.3 MPa) on the yield of MCS at DCS feed rates of 0.1, 0.2, and 0.3 kg/h, as shown in Figure 2. Reaction pressures were adjusted by feeding nitrogen, ensuring that changes in pressure did not affect the DCS concentration. Moreover, Figures S1 and S2 show the DCS consumption, the relative conversion of MCS under the same reaction conditions, respectively. In addition, the detailed experimental results are shown in Table S1.

As shown in Figure 2, at the feed rate of 0.1 kg/h, the MCS yield increased with temperature, while pressure had a minimal effect. At the feed rate of 0.2 kg/h, the yield exhibited a different trend compared to Figure 2a. It initially increased and then decreased with rising temperature, while it decreased and then increased with rising pressure, forming the saddle-shaped response surface. At 323.15 K and 0.3 MPa, the MCS yield reached the maximum value of 14.12 mol %. When the feed rate was 0.3 kg/h, the sensitivity of the MCS yield to temperature increased. The yield was generally higher at 313.15 and 323.15 K. Particularly at 0.3 MPa, when the temperature was raised from 303.15 to 313.15 K, the yield increased by 3.52 mol %, which corresponds to an increase of 62.23%.

In summary, the experiments conducted in this study demonstrated that appropriate temperatures, such as 313.15 or 323.15 K, were conducive to the formation of MCS. At the higher feed rate of 0.3 kg/h and elevated pressure of 0.3 MPa, the MCS yield exhibited significant sensitivity to temperature, resulting in substantial variations in yield. Therefore, in practical production, it is advisible to avoid increasing pressure under high feed rate conditions. The maximum MCS yield was achieved at 0.2 kg/h, 323.15 K, and 0.3 MPa. These trends suggested the presence of dual temperature-related effects and pressure- or volume-dependent reactions within the DCS disproportionation system. Additionally, the comparison of the three panels in Figure 2 revealed that the maximum MCS yield under different reaction conditions was only 14.11 mol %. This suggests that the disproportionation of DCS catalyzed by Amberlyst A21 likely involved numerous side reactions, which significantly interfered with the formation of MCS. Besides, significant variations in the yield growth trends under different feed rates highlighted the complexity of the DCS disproportionation reaction system and the multiple factors influencing it.

These findings underscored the need for an in-depth investigation into the reaction mechanism to provide insights for improving the catalytic disproportionation process and guiding new catalyst design strategies. However, due to the limitations of current experimental techniques, the toxic, flammable, and explosive nature of the reaction system posed significant safety risks during material transport and experimental detection. Moreover, it was challenging to identify an in situ detection method that could ensure safety while isolating the system from water and air. Under these circumstances, this study adopted the greener, safer, and more cost-effective approach, employing DFT calculations to investigate the mechanism at the atomic and molecular scales.

The DFT calculations were performed on the reaction process between $CH_3C_6H_4CH_2N(CH_3)_2$ and DCS at 333.15 K. The charges, spin multiplicities, and coordinates of all structures in DFT calculations are shown in the DFT Calculation Results section in Supporting Information. Besides, the Gibbs free energies for all molecules in the reaction are shown in Table S2. Initially, the analysis of the electrostatic potential surfaces (Figure 3) of $CH_3C_6H_4CH_2N(CH_3)_2$ and

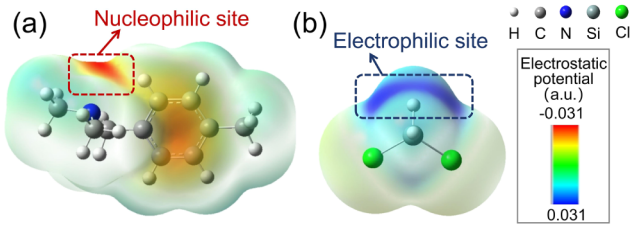

Figure 3. Electrostatic potential surfaces of $CH_3C_6H_4CH_2N(CH_3)_2$ (a) and DCS (b). (Negative electrostatic potential regions and positive electrostatic potential regions were marked in deep red and blue, respectively.)

DCS was conducted to determine the reactive sites. The nitrogen in $CH_3C_6H_4CH_2N(CH_3)_2$ exhibited the most negative electrostatic potential, making it the nucleophilic site; the adjacent hydrogen positions in DCS exhibited the most positive electrostatic potential, serving as electrophilic sites. Thus, the N in $CH_3C_6H_4CH_2N(CH_3)_2$ and the H in DCS were most likely to react.

The calculations revealed that the initial reaction between $CH_3C_6H_4CH_2N(CH_3)_2$ and DCS was the proton transfer process, and the initial states (IS), transition states (TS), and final states (FS) during the reaction are illustrated in R1 of Figure 4. This R1 reaction overcame the Gibbs free energy barrier of 119.10 kJ/mol, resulting in the formation of $CH_3C_6H_4CH_2(CH_3)_2NH^+$ and $SiHCl_2^-$. In Figure 4a, the relative Gibbs free energy variation for the R1 indicated the higher forward reaction barrier and the lower reverse barrier, making the reverse proton transfer from $CH_3C_6H_4CH_2(CH_3)_2NH^+$ to $SiHCl_2^-$ more feasible. This was identified as one of the significant impediments to the synthesis of MCS.

Subsequently, possible reactions in the presence of $SiHCl_2^-$ and DCS were considered (R2−5 in Figure 4). The R2 reaction occurred with the proton transfer between DCS and $SiHCl_2^-$ overcoming the energy barrier of 68.26 kJ/mol (R2 in Figure 4b) to produce $SiHCl_2^-$ and DCS. This reaction process demonstrated that the proton transfer could occur between chlorosilane molecules and chlorosilane ions, but no new product was produced by the R2. The R3 reaction underwent the chlorine transfer between DCS and $SiHCl_2^-$, overcoming the energy barrier of 138.08 kJ/mol (R3 in Figure 4b), resulting in $SiHCl_3$ (TCS) and SiH_2Cl^-.

In Figure 4, both the R4 and R5 commenced with DCS and $SiHCl_2^-$ as reactants, spontaneously forming structures with Si−Si bonds ($\Delta G(R5) < \Delta G(R4) < 0$), yet generated different products. The FS of R4 was $SiHCl_2$−$SiH_2Cl_2^-$, but the FS of R5 was $SiHCl_2$−SiH_2Cl and Cl^-. The differences in the products of R4 and R5 were attributed to the varying orientations of the reactants (DCS and $SiHCl_2^-$). Dual descriptor isosurface maps further elucidated the underlying reasons for these reactions,[39] as shown in Figure 4c. In these maps, regions prone to electron loss in DCS and $SiHCl_2^-$ were highlighted in blue, while those likely to gain electrons were marked in green. The regions (i) near Si in DCS tended to gain electrons, serving as the electrophilic site. Conversely, the region (ii) near Si of $SiHCl_2^-$ was susceptible to electron loss and was the nucleophilic site. Consequently, DCS and $SiHCl_2^-$ were capable of forming Si−Si bonds. In the R4 reaction, the bare Si of $SiHCl_2^-$ was oriented toward the H−H−Cl side of the DCS, and regions (ii) and (iii) were attracted to each other so that the Cl of the FS in R4 did not detach. In contrast, in

https://doi.org/10.1021/acsomega.4c11528
ACS Omega 2025, 10, 19480−19490

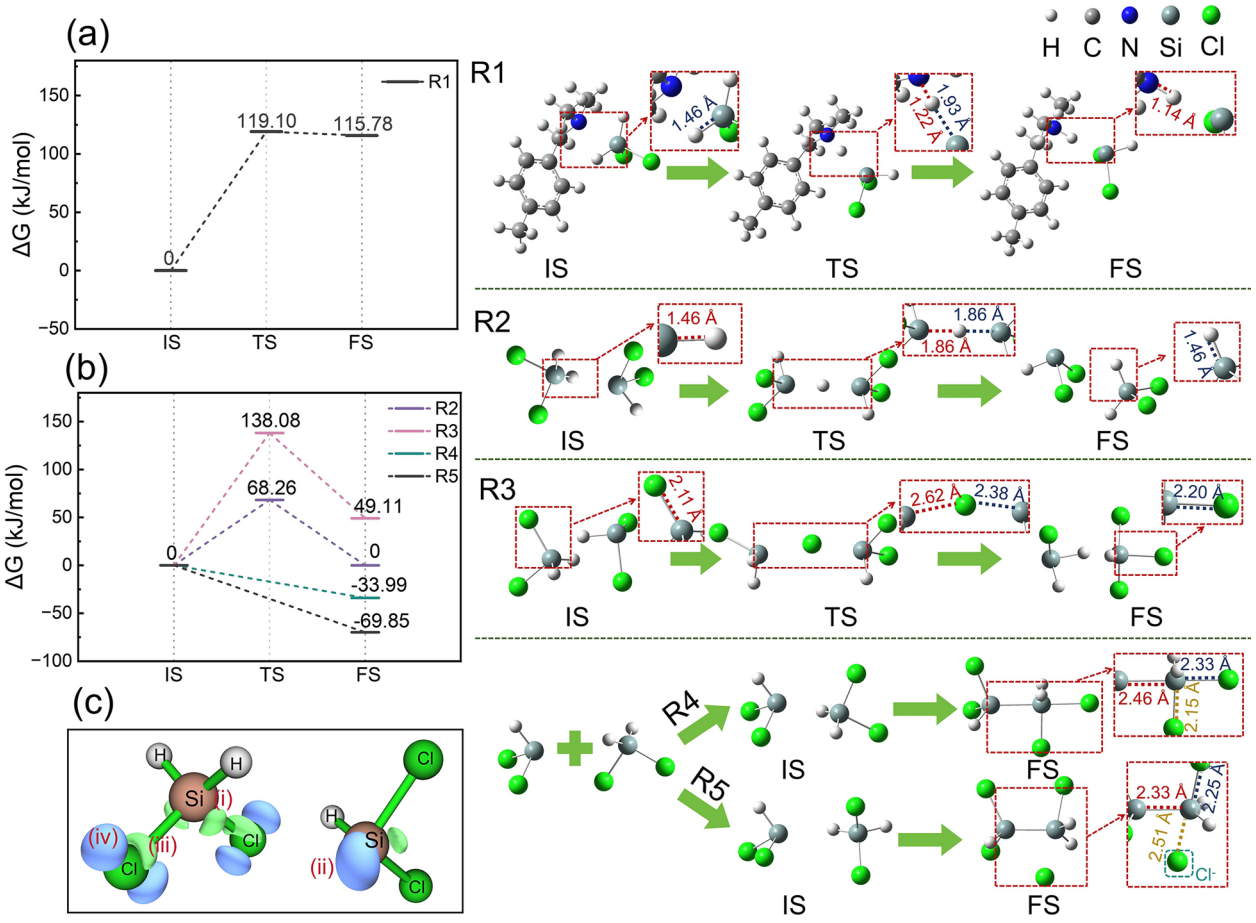

Figure 4. (a) Relative Gibbs free energy change of R1 from IS to FS, (b) relative Gibbs free energy changes of R2−R5 from IS to FS, (c) the dual descriptor isosurfaces for DCS and $SiHCl_2^-$ (iso = 0.014, with blue regions indicating areas prone to electron loss and green regions indicating areas prone to electron gain), and the reaction pathways of R1 to R5 at 333.15 K.

the R5, the bare Si in $SiHCl_2^-$ faced the H−Cl−Cl side of DCS, causing repulsion between regions (ii) and (iv), resulting in the detachment of Cl^- in the FS of R5. Moreover, the extensive overlap between regions (i) and (ii) in the R5 reaction signified the stronger interaction between the Si atoms, facilitating the reaction and lowering the energy barrier. Reactions R2−R5 produced various products, increasing the complexity of the reaction system.

The FS of R4 in Figure 4 and the IS of R7 in Figure 5 had the same structure, and the FS of R5 and the IS of R6 had the same structure, i.e., R4 and R7 were reactions occurring one after the other, and likewise, R5 and R6 were successive reactions. The upper Cl was transferred to the lower position through the twist of the dihedral angle. The repulsive effect of this Cl, which came by twisting, on the Cl^- below led to the connection of the Cl^- below to the Si on the left side, generating $SiHCl_3{-}SiH_2Cl^-$. This process overcame the energy barrier of 13.18 kJ/mol (R6 in Figure 5a). In the R7 reaction, an energy barrier of 23.81 kJ/mol was overcome (R7 in Figure 5a), leading to the formation of $SiHCl_3{-}SiH_2Cl^-$. Comparing R6 and R7, the essence of both reactions was intramolecular chlorine transfer, driven by the repulsion between Cl atoms, with $SiHCl_3{-}SiH_2Cl^-$ being the product of both reactions. However, the R6 reaction took place mainly through the twisting of dihedral angles, hence the lower energy barrier, making the reaction relatively easier. Subsequently, the product ($SiHCl_3{-}SiH_2Cl^-$) from R6 and R7 could participate in the formation processes of TCS and MCS (R9), making $SiHCl_3{-}SiH_2Cl^-$ the crucial intermediate. Nevertheless, $SiHCl_3{-}SiH_2Cl^-$ could also decompose (e.g., R8), releasing Cl^- and forming $SiHCl_2{-}SiH_2Cl$. Notably, the highest energy barrier required to release Cl^- in the R8 was 7.12 kJ/mol (R8 in Figure 5a), corresponding to the energy barrier for breaking the shortest Si−Cl bond with the length of 2.12 Å and releasing Cl^-.

The complexity of the chlorosilane disproportionation system was due not only to the presence of many reversible side reactions that could occur in succession but also to the interference of byproducts (e.g., Cl^-) with the main reaction. The R9 in Figure 5 was pivotal for the synthesis of MCS and TCS, yet it was beset by side reactions (e.g., R10) with considerably lower energy barriers. During the R9 reaction, the process of transferring the proton from $CH_3C_6H_4CH_2(CH_3)_2NH^+$ to $SiHCl_3{-}SiH_2Cl^-$ overcame the energy barrier of 31.52 kJ/mol (R9 in Figure 5b). However, in the R10 reaction, the Cl^- in $SiHCl_3{-}SiH_2Cl^-$ was electrostatically attracted to the H^+ in $CH_3C_6H_4CH_2(CH_3)_2NH^+$. This reaction produced $CH_3C_6H_4CH_2(CH_3)_2NH^+{\cdots}Cl^-$ and $SiHCl_2{-}SiH_2Cl$, with the notable decrease in Gibbs free energy by 124.37 kJ/mol (R10 in Figure 5b). Consequently, Cl^- readily dissociated from $SiHCl_3{-}SiH_2Cl^-$ and combined with $CH_3C_6H_4CH_2(CH_3)_2NH^+$, thereby impeding the production of MCS.

https://doi.org/10.1021/acsomega.4c11528
ACS Omega 2025, 10, 19480−19490

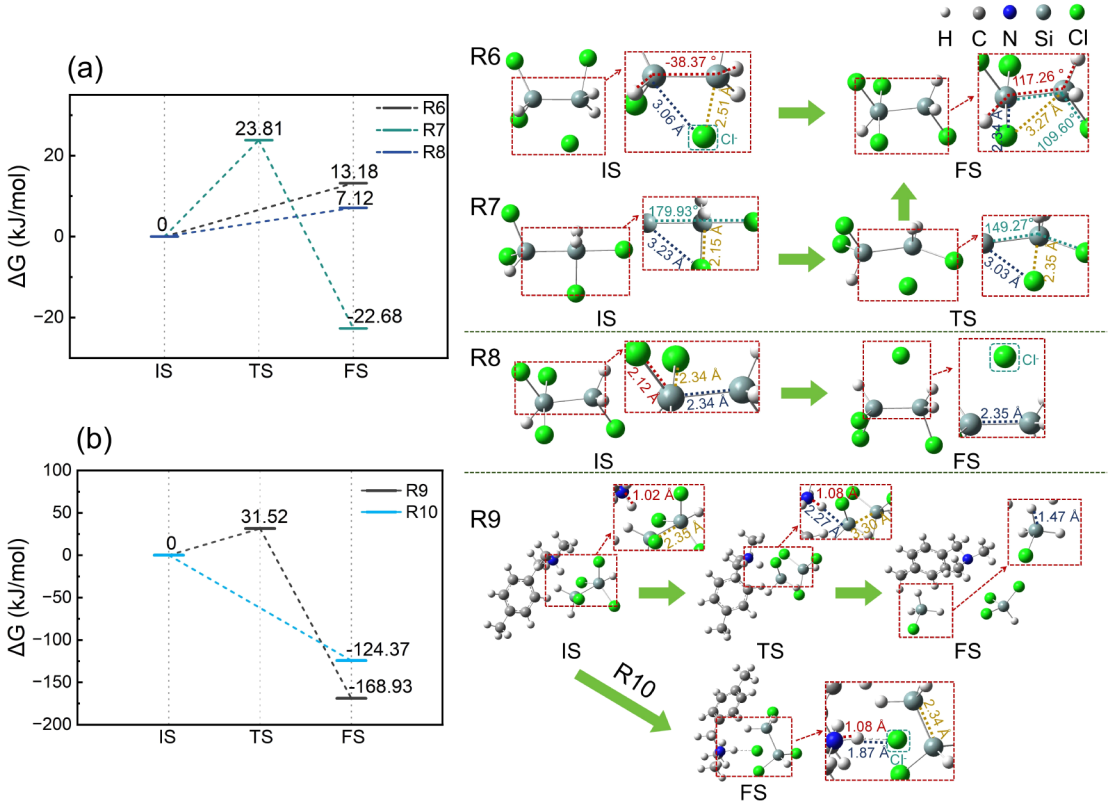

Figure 5. (a) Relative Gibbs free energy changes of R6−R8 from IS to FS, (b) relative Gibbs free energy changes of R9−R10 from IS to FS, and the reaction pathways from R6 to R10 at 333.15 K.

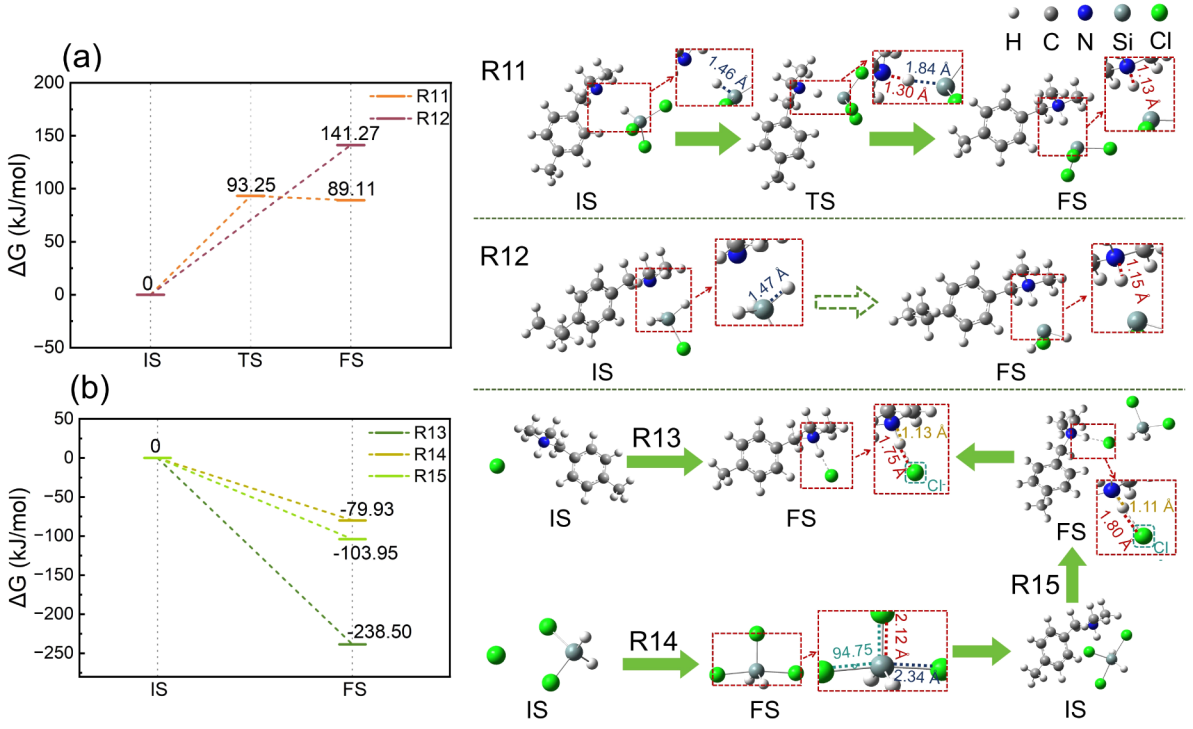

Figure 6. (a) Relative Gibbs free energy changes of R11−R12 from IS to FS, (b) relative Gibbs free energy changes of R13−R15 from IS to FS, and the reaction pathways from R11 to R15 at 333.15 K.

Indeed, MCS and TCS were not the terminal products in the chlorosilane disproportionation system. Instead, they underwent the proton transfer reactions similar to R1, as R11 and R12 in Figure 6. The R11 reaction surmounted the energy barrier of 93.25 kJ/mol (R11 in Figure 6a), ultimately yielding $CH_3C_6H_4CH_2(CH_3)_2NH^+$ and $SiCl_3^-$. In the R12 reaction, the H^+ was captured by N, eventually producing $CH_3C_6H_4CH_2(CH_3)_2NH^+$ and SiH_2Cl^-. The process neces-

https://doi.org/10.1021/acsomega.4c11528
ACS Omega 2025, 10, 19480−19490

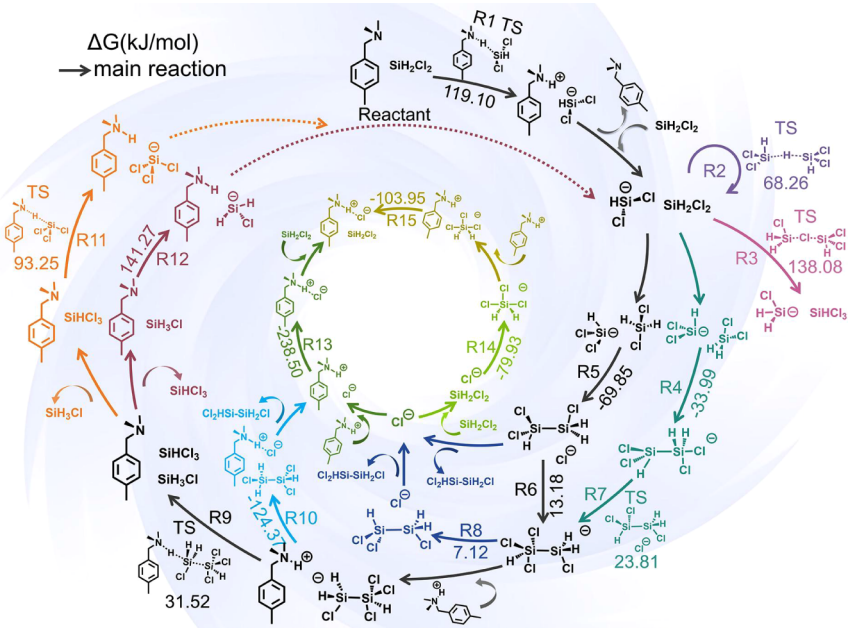

Figure 7. DCS catalytic disproportionation cycle pathways and relative Gibbs free energy barriers for R1 to R15 at 333.15 K. (The main reaction path is indicated by black arrows.)

Table 1. Reaction Equations for R1 to R15

Reaction	Equations
R1	$CH_3C_6H_4CH_2N(CH_3)_2 + SiH_2Cl_2 \leftrightarrow CH_3C_6H_4CH_2(CH_3)_2NH^+ + SiHCl_2^-$
R2	$SiHCl_2^- + SiH_2Cl_2 \leftrightarrow SiH_2Cl_2 + SiHCl_2^-$
R3	$SiHCl_2^- + SiH_2Cl_2 \leftrightarrow SiH_2Cl^- + SiHCl_3$
R4	$SiHCl_2^- + SiH_2Cl_2 \leftrightarrow SiHCl_2 - SiH_2Cl_2^-$
R5	$SiHCl_2^- + SiH_2Cl_2 \leftrightarrow SiHCl_2 - SiH_2Cl + Cl^-$
R6	$SiHCl_2 - SiH_2Cl + Cl^- \leftrightarrow SiHCl_3 - SiH_2Cl^-$
R7	$SiHCl_2 - SiH_2Cl_2^- \leftrightarrow SiHCl_3 - SiH_2Cl^-$
R8	$SiHCl_3 - SiH_2Cl^- \leftrightarrow SiHCl_2 - SiH_2Cl + Cl^-$
R9	$CH_3C_6H_4CH_2(CH_3)_2NH^+ + SiHCl_3 - SiH_2Cl^- \leftrightarrow SiH_3Cl + SiHCl_3$
R10	$CH_3C_6H_4CH_2(CH_3)_2NH^+ + SiHCl_3 - SiH_2Cl^- \rightarrow CH_3C_6H_4CH_2(CH_3)_2NH^+\cdots Cl^- + SiHCl_2 - SiH_2Cl$
R11	$CH_3C_6H_4CH_2N(CH_3)_2 + SiHCl_3 \leftrightarrow CH_3C_6H_4CH_2(CH_3)_2NH^+ + SiCl_3^-$
R12	$CH_3C_6H_4CH_2N(CH_3)_2 + SiH_3Cl \leftrightarrow CH_3C_6H_4CH_2(CH_3)_2NH^+ + SiH_2Cl^-$
R13	$CH_3C_6H_4CH_2(CH_3)_2NH^+ + Cl^- \rightarrow CH_3C_6H_4CH_2(CH_3)_2NH^+\cdots Cl^-$
R14	$SiH_2Cl_2 + Cl^- \rightarrow SiH_2Cl_3^-$
R15	$CH_3C_6H_4CH_2(CH_3)_2NH^+ + SiH_2Cl_3^- \rightarrow CH_3C_6H_4CH_2(CH_3)_2NH^+\cdots Cl^- + SiH_2Cl_2$

sitated overcoming the energy barrier of 141.27 kJ/mol (R12 in Figure 6a).

As Cl^- ions were identified as highly competitive byproducts in the formation of MCS, participating in multiple reactions (R5−R6, R8, and R10), reactions related to Cl^- were systematically investigated (R13−R15 in Figure 6b). (1) Cl^- could react with $CH_3C_6H_4CH_2(CH_3)_2NH^+$ (R13): under electrostatic attraction, Cl^- was captured by H^+, resulting in the formation of $CH_3C_6H_4CH_2(CH_3)_2NH^+\cdots Cl^-$. The Gibbs free energy change of this process was −238.50 kJ/mol (R13 in Figure 6b). (2) Cl^- could also react with DCS (R14): driven by nucleophilic action, Cl^- was attracted to the Si nucleus, forming the symmetrically structured $SiH_2Cl_3^-$. The reaction's Gibbs free energy change was −79.93 kJ/mol (R14 in Figure 6b). (3) The R15 reaction facilitated the conversion of the R14 product into the R13 product through chlorine transfer, with the Gibbs free energy change of −103.95 kJ/mol. In the R15 reaction, Cl^- from $SiH_2Cl_3^-$ was attracted to the H^+ of $CH_3C_6H_4CH_2(CH_3)_2NH^+$, leading to the formation of $CH_3C_6H_4CH_2(CH_3)_2NH^+\cdots Cl^-$, thereby completing the reaction cycle of Cl^-. (4) The Gibbs free energy changes for reactions R13 to R15 were all negative, rendering these

https://doi.org/10.1021/acsomega.4c11528
ACS Omega 2025, 10, 19480−19490

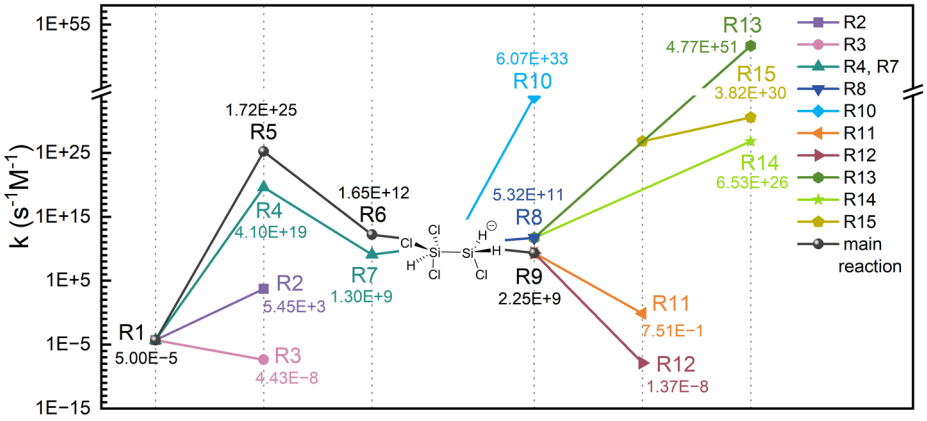

Figure 8. Reaction rate constants (k) of R1 to R15 at 333.15 K. The main reaction corresponds to the black curve.

reactions more likely to occur. In competitive reactions consuming DCS or $CH_3C_6H_4CH_2(CH_3)_2NH^+$, the reactions involving Cl^- (e.g., R13−R15), with lower Gibbs free energy changes, had advantages over other reactions with higher energy barriers, significantly disadvantaging the formation of MCS.

At 333.15 K, the DCS catalytic disproportionation cycle pathways and corresponding reaction equations for R1 to R15 are illustrated in Figure 7 and Table 1. The relative Gibbs free energies, bond distances, and dihedral angles of the IS, TS, and FS for R1 to R15 are listed separately in Tables S3 and S4.

The cycle commenced with the proton transfer between DCS and $CH_3C_6H_4CH_2(CH_3)_2$ (R1), where $CH_3C_6H_4CH_2(CH_3)_2$ served as the temporary proton reservoir, transforming DCS into a more polar chlorosilane ion. Subsequently, the proton transfer, chlorine transfer, and Si−Si bond generation between chlorosilane molecules and ions took place (R2 to R5), diversifying the species present in the system and increasing the complexity of the reaction system. Disilicon compounds containing Si−Si bonds exhibited various forms, such as $SiHCl_2$−$SiH_2Cl_2^-$ (FS of R4), $SiHCl_2$−SiH_2Cl (FS of R5, R8, and R10), and $SiHCl_3$−SiH_2Cl^- (FS of R6 and R7), among which only $SiHCl_3$−SiH_2Cl^- was the key intermediate directly involved in the formation process of MCS. Comparing different reaction pathways leading to the formation of $SiHCl_3$−SiH_2Cl^-, the pathway of $SiHCl_2^-$ + DCS → R5 → R6 → $SiHCl_3$−SiH_2Cl^- exhibited the lower energy barrier, making it more favorable than the $SiHCl_2^-$ + DCS → R4 → R7 → $SiHCl_3$−SiH_2Cl^-. During the MCS formation process (R9), $CH_3C_6H_4CH_2(CH_3)_2NH^+$ provided the hydrogen source for $SiHCl_3$−SiH_2Cl^-, facilitating the cleavage of the Si−Si bond. Just like DCS, the products of the R9 (MCS and TCS) could also undergo proton transfer with $CH_3C_6H_4CH_2N(CH_3)_2$ (R11 and R12), generating different chlorosilane ions that joined the complex chlorosilane reaction system as new reactants. To examine the ability of chlorosilane ions to capture protons, the energy variation rules of different chlorosilane ions and $CH_3C_6H_4CH_2(CH_3)_2NH^+$ with increasing N−H bond length calculated by the method M062X-GD3/6-311+g(2d,p) are shown in Figure S3 and Table S5. The results indicated that SiH_3^- has the strongest proton affinity and is most likely to capture the proton of $CH_3C_6H_4CH_2(CH_3)_2NH^+$. At the same time, disilicon compounds such as $SiHCl_2$−$SiH_2Cl_2^-$ and $SiHCl_3$−SiH_2Cl^- readily released Cl^- (R5, R8, and R10), and Cl^- could spontaneously form more stable byproducts with DCS or $CH_3C_6H_4CH_2(CH_3)_2NH^+$, with $CH_3C_6H_4CH_2(CH_3)_2NH^+\cdots Cl^-$ being the most likely to form (R10 and R13).

Overall, the reaction pathway R1 → R5 → R6 → R9, which was characterized by the relatively low energy barrier, served as the main route for producing MCS and was highlighted with black arrows in Figure 7 (the colors corresponding to each reaction were consistent throughout Figures 4−8). The reaction process in the chlorosilane disproportionation system comprised two cycles: the primary cycle for MCS production (R1 to R12) and the secondary Cl-related cycle (R13 to R15). To maximize the yield of MCS, it was desirable to promote the primary cycle that produced MCS and suppress the secondary cycle that competed for reactants.

To compare the reaction ease of R1−15 and to determine the rate-determining step that limits MCS generation, the k of R1 to R15 at 333.15 K are shown in Figure 8. In this figure, each point corresponds to the k of the corresponding reaction, and the sequential order of points along the curve represents the sequence in which the corresponding reactions occur. In the main reaction pathway (R1 → R5 → R6 → R9), $k(R1)$ was the lowest, making R1 the rate-determining step for MCS formation. Comparing the three reactions that essentially involved proton transfer between chlorosilanes and $CH_3C_6H_4CH_2N(CH_3)_2$ (R1, R11, and R12), it was observed that $k(R11) > k(R1) > k(R12)$. This indicated that the proton transfer with TCS (R11) occurred most readily, while the reaction with MCS (R12) was more challenging, suggesting that chlorosilanes with more hydrogen atoms were less likely to undergo proton transfer. Comparing the reaction processes between DCS and $SiHCl_2^-$ (R2−R5), the rate constants followed the order $k(R5) > k(R4) > k(R2) > k(R3)$. This suggested that DCS and $SiHCl_2^-$ more readily formed disilicon compounds (R5 and R4), with the R5 (forming $SiHCl_2$−SiH_2Cl and Cl^-) being the easiest to occur, and the chlorine transfer (R3) between DCS and $SiHCl_2^-$ being the most challenging. Comparing the R6 and R7, which yielded the significant intermediate $SiHCl_3$−SiH_2Cl^- as the product, $k(R6) > k(R7)$. The difference in their rates was attributed to the R6 facilitating intramolecular chlorine transfer by twisting the dihedral angle, thus occurring more readily. In the comparison of three reactions (R8−R10) utilizing $SiHCl_3$−SiH_2Cl^- as the reactant, the order of reaction rates was $k(R10) > k(R8) > k(R9)$. Therefore, the R10, leading to the formation of $CH_3C_6H_4CH_2(CH_3)_2NH^+\cdots Cl^-$ and $SiHCl_2$−SiH_2Cl, proceeded more easily, while the critical reaction for MCS

https://doi.org/10.1021/acsomega.4c11528
ACS Omega 2025, 10, 19480−19490

production (R9) occurred with difficulty. Consequently, the proportion of $SiHCl_3$−SiH_2Cl^- involved in MCS formation was relatively low. Comparing the three reactions involving Cl^- (R13−15), the order of reaction rates was $k(R13) > k(R15) > k(R14)$. Thus, the reactions leading to the formation of $CH_3C_6H_4CH_2(CH_3)_2NH^+\cdots Cl^-$ occurred more readily (R13 and R15), while the formation of $SiH_2Cl_3^-$ was comparatively difficult (R14), but still easier than the main reaction. Furthermore, reactions involving Cl^- exhibited higher rate constants, such as R5, R6, R8, R10, and R13 to R15. In the R5 and R6, Cl^- provided the chlorine source for the formation of $SiHCl_3$−SiH_2Cl^-, facilitating the production of MCS. However, in R8, R10, and R13 to R15, the Cl^- released tended to react with $SiHCl_3$−SiH_2Cl^-, $CH_3C_6H_4CH_2(CH_3)_2NH^+$ or DCS, which was not conducive to the formation of MCS.

In addition to calculating the ΔG and k, the enthalpy changes (ΔH) of reactions R1−15 at 333.15 K were analyzed, as summarized in Table S6. In the primary cycle, $\Delta H(R1)$ = 120.24 kJ/mol >0, indicating that the rate-determining step (R1) was endothermic. In contrast, in the secondary cycle, $\Delta H(R13) = -233.46$ kJ/mol < $\Delta H(R14) = -88.33$ kJ/mol ≈ $\Delta H(R15) = -87.75$ kJ/mol < 0, demonstrating that R13−R15 were exothermic. Therefore, increasing the reaction temperature enhanced $k(R1)$, shifting the chemical equilibrium of R1 in the forward direction. Furthermore, the trends observed in Figures S4 and S5, obtained through DFT calculations, demonstrated that the ΔG of R1 decreased linearly and the k increased exponentially with rising temperature. These trends not only align with eq 4 but also illustrate the temperature-dependent behavior of the R1 reaction. Meanwhile, for reactions that interfered with MCS formation (e.g., R13−R15), the higher temperature promoted the reverse shift of their chemical equilibria. These findings indicated that elevated temperatures facilitated the increase in MCS yield. However, excessively high temperatures also accelerated the disproportionation of MCS itself in R12, consuming the produced MCS and ultimately reducing its yield. This analysis explained the observed trend where MCS yield increased initially but decreased as the temperature rose further. Combined with Figure 2, the optimal temperature for maximizing MCS yield was determined to be 313.15 or 323.15 K.

Although pressure adjustment via N_2 did not alter the thermodynamic equilibria, the compressed high-pressure gas enhanced heat transfer. This intensified the coupling between temperature control and reaction kinetics. Consequently, under high feed rates and elevated pressure conditions, the MCS yield became more susceptible to temperature perturbations. These insights aligned with the experimental observations.

In summary, in the MCS generation process, the R1 with the lowest rate constant was identified as the rate-determining step. Consequently, to enhance the yield of MCS, it was imperative to increase the $k(R1)$ by modifying the reaction conditions. In the case of the R12, the disproportionation reaction consumed MCS produced by R9, which negatively impacted the yield of MCS. Moreover, even though $k(R12)$ was the lowest among all reactions, the role of elevated temperature in enhancing $k(R2)$ could not be ignored. The influence of Cl^- needed to be assessed from two perspectives: first, Cl^- acted as the chlorine source for the formation of $SiHCl_3$−SiH_2Cl^-, and second, Cl^- was the highly competitive byproduct in the generation of MCS, consuming DCS, $CH_3C_6H_4CH_2(CH_3)_2NH^+$, and the important intermediate ($SiHCl_3$−SiH_2Cl^-). It was necessary to limit the detachment of Cl^- from the reaction system of disilicon compounds and to prevent the excessive production of Cl^-. Hence, managing the concentration and activity of Cl^- within the reaction system was vital for improving the yield of MCS and minimizing undesirable side reactions. These insights aid in the targeted design of catalysts to enhance reaction efficiency and selectivity. Besides, understanding the interactions between catalysts and reactants optimizes the formulation and structure of the catalysts, thereby increasing their catalytic activity and stability.

Finally, to validate the reliability of the computational setup, it is necessary to compare the computational results with experimental values. However, due to the safety risks and lack of immediate detection equipment associated with conducting the DCS disproportionation experiment, and the lack of available experimental data in the literature, TCS disproportionation, which had more reference data, was considered instead. Therefore, only the computational results and experimental data for the TCS disproportionation process were discussed. The reaction equations and ΔG for the TCS disproportionation process by DFT calculations in this work are presented in Table S7, where the rate-determining step was the TCS dehydrogenation (TCS-R1, same as R11) process. Besides, the ΔG and k calculated by DFT in this work for TCS-R1 at 303.15, 333.15, and 363.15 K are shown in Table S8. According to the Arrhenius equation, the exponential relationship exists between the reaction rate constant and temperature. The experimental data for TCS disproportionation were obtained through the literature.[16,40] The experimentally derived k for TCS disproportionation in the gas phase[40] and liquid phase[16] are plotted on the Arrhenius diagram in Figure 9, alongside the k for TCS-R1 obtained from DFT calculations in this work. The Arrhenius parameters for the liquid-phase[16] and gas-phase[40] reactions of trichlorosilane disproportionation, along with TCS-R1 derived from DFT calculations in this work, are presented in Table S9. In Figure 9, the k for TCS-R1

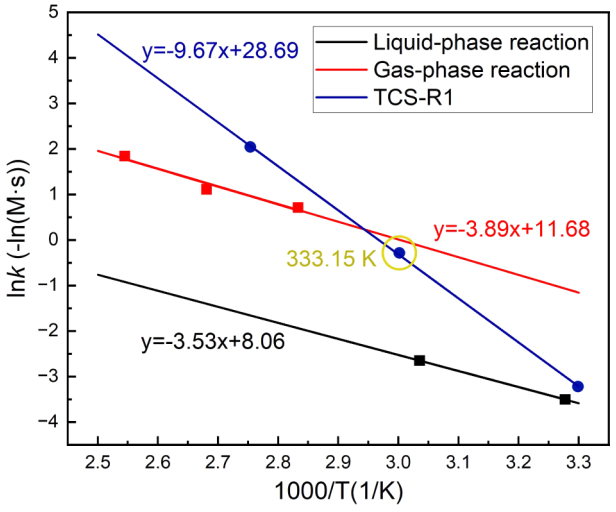

Figure 9. k for TCS disproportionation in the gas phase and liquid phase are plotted on the Arrhenius diagram, alongside the k for TCS-R1. Among these, the square points representing the ln k values for the gas-phase and liquid-phase reactions were obtained from experiments reported in references,[16,40] while the round points representing the ln k values for TCS-R1 were derived from DFT calculations in this work.

https://doi.org/10.1021/acsomega.4c11528
ACS Omega 2025, 10, 19480−19490

at 333.15 and 363.15 K were close to the corresponding k for the gas-phase reaction, especially at 333.15 K. This supported the rationale for setting 333.15 K as the computational temperature. At 303.15 K, which was close to the boiling point of TCS (about 305.15 K), the corresponding k aligned more closely with the liquid-phase reaction. In summary, the k for TCS-R1, determined through DFT calculations, exhibited excellent agreement with the experimental data. This conclusion validated the rationality of the computational methodology and confirmed that chlorosilane dehydrogenation was the rate-determining step of the disproportionation process, exerting a significant influence on the overall reaction.

4. CONCLUSIONS

Here, through experiments and DFT calculations, this research investigated the factors influencing MCS yield, the reaction cycle mechanisms, and key intermediates in the DCS disproportionation reaction. It was found that, as the feed rate increased, the DCS disproportionation required more precise temperature control and exhibited significantly enhanced sensitivity at high pressure. Moreover, under the conditions of 0.2 kg/h, 323.15 K, and 0.3 MPa, the MCS yield reached the maximum of 14.12 mol %. Besides, the proposed reaction cycle mechanisms effectively explained the complexity of the MCS yield variations. The results demonstrated that the dehydrogenation reaction of DCS, as the rate-determining step in the DCS disproportionation, exhibited antagonism with the disproportionation of MCS itself. This antagonistic interaction led to the MCS yield first increasing and then decreasing with rising temperature. These findings provide important theoretical insights for efficiently increasing MCS yield in industrial applications and for designing catalysts tailored to chlorosilane disproportionation reactions in the future.

■ ASSOCIATED CONTENT

Supporting Information

The Supporting Information is available free of charge at https://pubs.acs.org/doi/10.1021/acsomega.4c11528.

Experimental results, the DFT calculation results, the diagrams, charges, spin multiplicities and coordinates of the initial state (IS), transition state (TS), and final state (FS) in R1−R15 (PDF)

■ AUTHOR INFORMATION

Corresponding Authors

Qiuyun Mao − *Department of Educational Science, Hunan First Normal University, Changsha 410205, PR China*; Email: qiuyun91@hnfnu.edu.cn

Ye Wan − *Luoyang China Silicon Corporation Ltd., Luoyang 471024, PR China; National Engineering Research Center of Silicon-based Materials Manufacturing Technology, Luoyang 471023, PR China*; Email: wany@sinosico.com

Qifan Zhong − *School of Metallurgy and Environment, Central South University, Changsha 410083, PR China*; orcid.org/0000-0003-4963-0516; Email: 348259246@qq.com, zhongqifanchina@csu.edu.cn

Authors

Ke Sun − *School of Metallurgy and Environment, Central South University, Changsha 410083, PR China*

Jianyun Zheng − *State Key Laboratory of Chem/Bio-Sensing and Chemometrics, College of Chemistry and Chemical Engineering, Hunan University, Changsha 410082, PR China*; orcid.org/0000-0002-2262-7694

Jianhua Liu − *State Key Lab of Silicon and Advanced Semiconductor Materials, School of Materials Science and & Engineering, Zhejiang University, Hangzhou 310027, PR China; Luoyang China Silicon Corporation Ltd., Luoyang 471024, PR China*

Zhenjun Yuan − *Luoyang China Silicon Corporation Ltd., Luoyang 471024, PR China; National Engineering Research Center of Silicon-based Materials Manufacturing Technology, Luoyang 471023, PR China*

Guangan Gu − *Shanghai Jingmeng Silicon Materials Corporation Ltd., Shanghai 201707, PR China*

Guopeng Li − *Nanjing Guosheng Electronics Corporation Ltd., Nanjing 211100, PR China*

Complete contact information is available at: https://pubs.acs.org/10.1021/acsomega.4c11528

Notes

The authors declare no competing financial interest.

■ ACKNOWLEDGMENTS

This work was supported by the National Natural Science Foundation of China (Nos. 52174338, 52374421, and 52404318), the Science and Technology Innovation Program of Hunan Province (2024RC3039), the Young Elite Scientists Sponsorship Program by CAST, China (No. YESS20210258), the Central South University Innovation-Driven Research Programme (No. 2023CXQD005), the Education Department of Hunan Provincial Government (23B0841), the Yunnan Province Science and Technology Planning Project No. 202202AB080017, and the Guizhou Provincial Science and Technology Projects No.[2023]General212. This work was supported in part by the High-Performance Computing Center of Central South University, the National Engineering Research Centre of Low-carbon Nonferrous Metallurgy, and the XIAOMI Foundation.

■ REFERENCES

(1) Vulovic, B.; Cinderella, A. P.; Watson, D. A. Palladium-Catalyzed Cross-Coupling of Monochlorosilanes and Grignard Reagents. *ACS Catal.* **2017**, *7* (12), 8113−8117.

(2) Guan, W.; Lu, L.; Jiang, Q.; Gittens, A. F.; Wang, Y.; Novaes, L. F. T.; Klausen, R. S.; Lin, S. An Electrochemical Strategy to Synthesize Disilanes and Oligosilanes from Chlorosilanes. *Angew. Chem. Int. Ed.* **2023**, *62* (26), No. e202303592.

(3) Tomasini, P.; Weeks, K. D. Monochlorosilane for Low Temperature Silicon Epitaxy. *J. Electrochem. Soc.* **2011**, *158* (5), H604−H608.

(4) Kim, H. S.; Hwang, S. M.; Meng, X.; Byun, Y. C.; Jung, Y. C.; Ravichandran, A. V.; Sahota, A.; Kim, S. J.; Ahn, J.; Lee, L. High growth rate and high wet etch resistance silicon nitride grown by low temperature plasma enhanced atomic layer deposition with a novel silylamine precursor. *J. Mater. Chem. C* **2020**, *8* (37), 13033−13039.

(5) Ovanesyan, R. A.; Filatova, E. A.; Elliott, S. D.; Hausmann, D. M.; Smith, D. C.; Agarwal, S. Atomic layer deposition of silicon-based dielectrics for semiconductor manufacturing: Current status and future outlook. *J. Vac. Sci. Technol., A* **2019**, *37* (6), 060904.

(6) Ramírez-Márquez, C.; Sánchez-Ramírez, E.; Quiroz-Ramírez, J. J.; Gómez-Castro, F. I.; Ramírez-Corona, N.; Cervantes-Jauregui, J. A.; Segovia-Hernández, J. G. Dynamic behavior of a multi-tasking reactive distillation column for production of silane, dichlorosilane and monochlorosilane. *Chem. Eng. Process* **2016**, *108*, 125−138.

(7) Yaws, C. L.; Jelen, F. C.; Li, K.-Y.; Patel, P. M.; Fang, C. S. New technologies for solar energy silicon: Cost analysis of UCC Silane Process. *Sol. Energy* **1979**, *22* (6), 547−553.
(8) Xu, W. Y.; Cheng, Z. H.; Mo, L. B.; Si, H. T.; Shen, M. S.; Peng, J. X.; Fang, Z. L.; Liao, M. Y.; Chen, X. Mechanistic investigations of the disproportionation reaction catalyzed by AlCl/NH-MIL-53(Al) to produce dimethyldichlorosilane. *Silicon* **2024**, *16* (4), 1795−1807.
(9) Xu, W. Y.; Mo, L. B.; Cheng, Z. H.; Si, H. T.; Shen, M. S.; Fang, Z. L.; Peng, J. X.; Liao, M. Y.; Chen, X. Mechanism of dimethyldichlorosilane preparation by NH-MIL-53(Al) @γ-AlO core-shell catalyst before and after AlCl modification. *J. Solid State Chem.* **2024**, *331*, 124529.
(10) Xu, W. Y.; Si, H. T.; Mo, L. B.; Cheng, Z. H.; Huang, H. K.; Peng, J. X.; Chen, X.; Liao, M. Y. Preparation of KAlCl4/ZSM-5@ γ-Al2O3 hollow core-shell catalyst and its study on the disproportionation of methylchlorosilanes. *J. Solid State Chem.* **2024**, *332*, 124561.
(11) Xu, W.; Yan, F.; Yang, S.; Guo, Z.; Hu, L.; He, Z.; Hong, S. Mechanism on The Disproportionating Synthesis of Dichlorodimethyl- silane by ZSM-5(5 T)@γ-Al2O3 Series Core-Shell Catalysts. *Appl. Organomet. Chem* **2020**, *34* (3), No. e5419.
(12) Huang, X.; Ding, W. J.; Yan, J. M.; Xiao, W. D. Reactive Distillation Column for Disproportionation of Trichlorosilane to Silane: Reducing Refrigeration Load with intermediate Condensers. *Ind. Eng. Chem. Res.* **2013**, *52* (18), 6211−6220.
(13) Schweizer, J. I.; Meyer, L.; Nadj, A.; Diefenbach, M.; Holthausen, M. C. Unraveling the Amine-Induced Disproportionation Reaction of Perchlorinated Silanes-A DFT Study. *Chem. - Eur. J.* **2016**, *22* (40), 14328−14335.
(14) Vorotyntsev, A. V.; Petukhov, A. N.; Makarov, D. A.; Sazanova, T. S.; Razov, E. N.; Nyuchev, A. V.; Mochalov, L. A.; Markov, A. N.; Kulikov, A. D.; Vorotyntsev, V. M. Supported ionic liquid-like phases based on CMS/DVB with different NR3 cations as catalysts for the chlorosilanes disproportionation. *Appl. Catal., B* **2018**, *239*, 102−113.
(15) Vorotyntsev, A. V.; Petukhov, A. N.; Makarov, D. A.; Razov, E. N.; Vorotyntsev, I. V.; Nyuchev, A. V.; Kirillova, N. I.; Vorotyntsev, V. M. Synthesis, properties and mechanism of the ion exchange resins based on 2-methyl-5-vinylpyridine and divinylbenzene in the catalytic disproportionation of trichlorosilane. *Appl. Catal., B* **2018**, *224*, 621−633.
(16) *Low Cost Solar Array Project. Feasibility of the silane process for producing semiconductor-grade silicon*; Union Carbide Corp., New York, USA, United States, 1979.
(17) Ring, M. A.; Jenkins, R. L.; Zanganeh, R.; Brown, H. C. New 1: 1 adduct of trimethylamine and trichlorosilane, trimethylammonium trichlorosilyl. *J. Am. Chem. Soc.* **1971**, *93*, 265−267.
(18) Vorotyntsev, A. V.; Petukhov, A. N.; Sazanova, T. S.; Pryakhina, V. I.; Nyuchev, A. V.; Otvagina, K. V.; Markov, A. N.; Atlaskina, M. E.; Vorotyntsev, I. V.; Vorotyntsev, V. M. Imidazolium-based SILLPs as organocatalysts in silane production: Synthesis, characterization and catalytic activity. *J. Catal.* **2019**, *375*, 427−440.
(19) Nelson, W. M.; Naidoo, P.; Ramjugernath, D. Phase equilibrium data for potentially hazardous binary mixtures involving dichlorosilane, trichlorosilane and silicon-tetrachloride. *J. Chem. Thermodyn.* **2015**, *91*, 420−426.
(20) Jain, A.; Shin, Y.; Persson, K. A. Computational predictions of energy materials using density functional theory. *Nat. Rev. Mater.* **2016**, *1* (1), 15004.
(21) Mao, Q. Y.; Pang, Y. J.; Li, X. C.; Chen, G. J.; Tan, H. W. Theoretical Study of the Mechanisms of Two Copper Water Oxidation Electrocatalysts with Bipyridine Ligands. *ACS Catal.* **2019**, *9* (9), 8798−8809.
(22) Liu, G. D.; Shih, A. J.; Deng, H. Q.; Ojha, K.; Chen, X. T.; Luo, M. C.; Mccrum, I. T.; Koper, M. T. M.; Greeley, J.; Zeng, Z. H. Site-specific reactivity of stepped Pt surfaces driven by stress release. *Nature* **2024**, *626* (8001), 1005.
(23) Xu, C. Y.; Zhang, Y. W.; Chen, J. C.; Lin, J. Y.; Zhang, X. H.; Wang, Z. H.; Zhou, J. H. Enhanced mechanism of the photo-thermochemical cycle based on effective Fe-doping TiO films and DFT calculations. *Appl. Catal., B* **2017**, *204*, 324−334.
(24) Boychuk, B. T. A.; Jeong, Y. E. R.; Wetmore, S. D. Assessment of the Accuracy of DFT-Predicted Li + −Nucleic Acid Binding Energies. *J. Chem. Theory Comput.* **2021**, *17* (8), 5392−5408.
(25) Xu, C. Y.; Zhang, Y. W.; Pan, F. Q.; Huang, W. H.; Deng, B. W.; Liu, J. Z.; Wang, Z. H.; Ni, M. J.; Cen, K. F. Guiding effective nanostructure design for photo-thermochemical CO conversion: From DFT calculations to experimental verifications. *Nano Energy* **2017**, *41*, 308−319.
(26) Coin, G.; Dubourdeaux, P.; Avenier, F.; Patra, R.; Castro, L.; Lebrun, C.; Bayle, P. A.; Pécaut, J.; Blondin, G.; Maldivi, P. Experiments and DFT Computations Combine to Decipher Fe-Catalyzed Amidine Synthesis through Nitrene Transfer and Nitrile Insertion. *ACS Catal.* **2021**, *11* (4), 2253−2266.
(27) Stanford, M. W.; Schweizer, J. I.; Menche, M.; Nichol, G. S.; Holthausen, M. C.; Cowley, M. J. Intercepting the Disilene-Silylsilylene Equilibrium. *Angew. Chem., Int. Ed.* **2019**, *58* (5), 1329−1333.
(28) Huang, G.-Q.; Sun, S.-S. Redistribution reactive distillation process for treating dichlorosilane. *Hua Xue Gong Cheng* **2014**, *42* (1), 19−23.
(29) Mueh, E.; Rauleder, H.; Lang, J. E.; Schork, R.; *Monochlorosilane, process and apparatus for the preparation thereof*. US 9,221,689 B2, 2015.
(30) Bogale, Y.; Neelaiah Babu, G. Amberlyst A21 catalyzed Morita-Baylis-Hillman reaction. *Curr. Res. Green Sustainable Chem.* **2021**, *4*, 100069.
(31) Gaussian Inc. *Gaussian 16 Rev. C.01*; Gaussian Inc., 2016.
(32) Qiu, C.; Chen, J.; Huan, F.; Deng, S.; Yao, Z.; Wang, S.; Wang, J. Curing and Cross-Linking Processes in the Poly(3,3-bis-azidomethyl oxetane)-tetrahydrofuran/Toluene Diisocyanate/Trimethylolpropane System: A Density Functional Theory and Accelerated ReaxFF Molecular Dynamics Investigation. *ACS Omega* **2024**, *9* (30), 33153−33161.
(33) Schreiner, P. R.; Reisenauer, H. P.; Allen, W. D.; Sattelmeyer, K. W. Triplet H−C−SiHCl2: Combined Matrix-IR and CCSD(T) Identification, and the Role of the Open-Shell Singlet State. *Org. Lett.* **2004**, *6* (7), 1163−1166.
(34) Prasad, S.; Rodene, D. D.; Burkholder, M. B.; Donald, K. J.; Gupton, B. F. Substituent Effects and the Energetics of Noncatalyzed Aryl Halide Aminations: A Theoretical Investigation. *ACS Omega* **2021**, *6* (41), 27216−27224.
(35) Narayanan, B.; Redfern, P. C.; Assary, R. S.; Curtiss, L. A. Accurate quantum chemical energies for 133 000 organic molecules. *Chem. Sci.* **2019**, *10* (31), 7449−7455.
(36) Sevinçek, R.; Aygün, M.; Şahin, Y. Enthalpy of formation calculations on five-membered azaborolidine derivatives. *J. Mol. Struct.* **2020**, *1217*, 128321.
(37) Fernández-Ramos, A.; Ellingson, B. A.; Meana-Pañeda, R.; Marques, J. M. C.; Truhlar, D. G. Symmetry numbers and chemical reaction rates. *Theor. Chem. Acc.* **2007**, *118* (4), 813−826.
(38) Lu, T.; Chen, F. W. Multiwfn: A multifunctional wavefunction analyzer. *J. Comput. Chem.* **2012**, *33* (5), 580−592.
(39) Cao, J. S.; Ren, Q.; Chen, F. W.; Lu, T. Comparative study on the methods for predicting the reactive site of nucleophilic reaction. *Sci. China: Chem.* **2015**, *58* (12), 1845−1852.
(40) Mochalov, G.; Stolmakov, Y.; Zhuchok, O. Thermodynamics and Kinetics of the Reaction of Catalytic Dismutation of Chlorosilanes in the Vapor Phase in the Temperature Range of 353−393 K. *ChemEngineering* **2023**, *7* (1), 13.

https://doi.org/10.1021/acsomega.4c11528
ACS Omega 2025, 10, 19480−19490